Astronomy
&
Astrophysics

The Crab pulsar in the 0.75–30 MeV range as seen by CGRO COMPTEL

A coherent high-energy picture from soft X-rays up to high-energy γ-rays

L. Kuiper[2], W. Hermsen[2], G. Cusumano[5], R. Diehl[1], V. Schönfelder[1], A. Strong[1],
K. Bennett[3], and M. L. McConnell[4]

[1] Max-Planck-Institut für Extraterrestrische Physik, 85741 Garching, Germany
[2] SRON – National Institute for Space Research, Sorbonnelaan 2, 3584 CA Utrecht, The Netherlands
[3] Astrophysics Division, European Space Research and Technology Centre, 2200 AG, Noordwijk, The Netherlands
[4] Space Science Centre, University of New Hampshire, Durham, NH 03824, USA
[5] Istituto di Fisica Cosmica ed Applicazioni all'Informatica CNR, Via U. La Malfa 153, 90146 Palermo, Italy

Abstract. We present the time-averaged characteristics of the Crab pulsar in the 0.75–30 MeV energy window using data from the imaging Compton Telescope COMPTEL aboard the Compton Gamma-Ray Observatory (CGRO) collected over its 9 year mission. Exploiting the exceptionally long COMPTEL exposure on the Crab allowed us to derive significantly improved COMPTEL spectra for the Crab nebula and pulsar emissions, and for the first time to accurately determine at low-energy γ-rays the pulse profile as a function of energy. These timing data, showing the well-known main pulse and second pulse at a phase separation of $\sim$0.4 with strong bridge emission, are studied together with data obtained at soft/hard X-ray energies from the ROSAT HRI, BeppoSAX LECS, MECS and PDS, at soft γ-rays from CGRO BATSE and at high-energy γ-rays from CGRO EGRET in order to obtain a coherent high-energy picture of the Crab pulsar from 0.1 keV up to 10 GeV. The morphology of the pulse profile of the Crab pulsar is continuously changing as a function of energy: the intensities of both the second pulse and the bridge emission increase relative to that of the first pulse for increasing energies up to $\sim$1 MeV. Over the COMPTEL energy range above 1 MeV an abrupt morphology change happens: the first pulse becomes again dominant over the second pulse and the bridge emission loses significance such that the pulse profile above 30 MeV is similar to the one observed at optical wavelengths. A pulse-phase-resolved spectral analysis performed in 7 narrow phase slices consistently applied over the 0.1 keV–10 GeV energy interval shows that the pulsed emission can empirically be described with 3 distinct spectral components: i) a power-law emission component (1 keV–5 GeV; photon index 2.022 ± 0.014), present in the phase intervals of the two pulses; ii) a curved spectral component required to describe soft ($\lesssim$100 keV) excess emission present in the same pulse-phase intervals; iii) a broad curved spectral component reflecting the bridge emission from 0.1 keV to $\sim$10 MeV. This broad spectral component extends in phase over the full pulse profile in an approximately triangular shape, peaking under the second pulse. Recent model calculations for a three-dimensional pulsar magnetosphere with outer magnetospheric gap acceleration by Cheng et al. (2000) appear at present most successful in explaining the above complex high-energy characteristics of the Crab pulsar.

Key words. pulsars: individual: PSR B0531+21 – stars: neutron – supernovae: individual: Crab nebula – gamma rays: observations – X-rays: stars

1. Introduction

The Crab pulsar (PSR B0531+21) has been studied extensively over the entire electromagnetic spectrum with pulse profiles dominated by two pulses, separated $\sim$0.4 in pulse phase and approximately aligned in absolute phase over all wavelengths.

After the first detections of pulsed emission in the X-ray regime by Fritz et al. (1969; $\sim$1–13 keV) and Bradt et al. (1969; 1.5–10 keV), the first significant detection of pulsed soft γ-ray emission was reported by Kurfess (1971; 100–400 keV). A great boost forward was made by the X-ray instruments aboard the OSO-8

(Pravdo & Serlemitsos 1981; 2–50 keV, revealing spectral variations of the pulsed emission as a function of pulse-phase), HEAO-1 (Knight 1982, 18–200 keV; introducing the possible existence of at least 2 pulsed emission components: one associated with the 2 main peaks and one with the bridge, the interval between the two peaks) and HEAO-2 (Einstein) satellites (Harnden & Seward 1984, 0.1–4.5 keV; producing the first high-resolution ($\sim4''$) image of the Crab nebula/pulsar in X-rays along with a high-resolution soft X-ray pulse profile). Recently, Pravdo et al. (1997) presented the details of a pulse-phase-resolved spectral analysis of the pulsed emission in the 5–200 keV interval based on RXTE PCA and HEXTE data. They found systematic spectral changes in the photon power-law index as a function of pulse-phase across the interval of the pulsed emission. Their work is confirmed by the findings presented by Massaro et al. (2000), who used data from the narrow field instruments aboard BeppoSAX (0.1–300 keV). These authors also made an attempt to disentangle the two emission components, introduced by Knight (1982), assuming for one component (reflecting the emission in the 2 peaks) the shape of the optical pulse profile and for the other component (the bridge emission) a shape from an analytical model with adjustable parameters.

At medium γ-ray energies the first detection of pulsed radiation (0.6–9 MeV) from the Crab pulsar was reported by Hillier et al. (1970); see also Walraven et al. (1975), Graser & Schönfelder (1982), Mahoney et al. (1984) and Agrinier et al. (1990).

In the high-energy γ-ray domain ($\gtrsim30$ MeV) the first indications for pulsed emission from the Crab pulsar were obtained from data collected by balloon-borne spark chambers or gas Cherenkov detector systems (see e.g. Browning et al. 1971; Albats et al. 1972; Parlier et al. 1973; McBreen et al. 1973). A big step forward in this energy range was made by the SAS-2 spark chamber experiment in the early seventies. In these data (20 MeV–1 GeV) significant pulsed emission was reported by Kniffen et al. (1974) and Thompson et al. (1977). The most detailed early information on the pulsed high-energy γ-ray properties of the Crab pulsar was, however, provided by the data from the European COS-B satellite (Bennett et al. 1977; Wills et al. 1982; Clear et al. 1987). Significant bridge emission was discovered in the combined COS-B Crab dataset, and the spectral characteristics of the pulsed and unpulsed (nebula) emission turned out to be quite diverse. Also, the alignment of the main pulse (P1) from the radio regime up to high-energy γ-rays was shown by Wills et al. (1982).

The launch of the Compton Gamma-Ray Observatory (CGRO; 20 keV–30 GeV) in April 1991 brought about an enormous improvement in the statistical quality of the γ-ray data. During its exceptionally long lifetime of more than 9 years Crab pulsar data were collected by the Energetic Gamma-Ray Experiment (EGRET; 20 MeV–30 GeV) showing clearly changing spectral behaviour as a function of pulse-phase

(Nolan et al. 1993; Fierro 1995; Fierro et al. 1998). The imaging Compton Telescope COMPTEL (0.75–30 MeV) viewed the Crab each time simultaneously with EGRET. The results based on data from an early set of observations performed during the first-year all-sky survey of the CGRO mission had been published by Much et al. (1995) and Carramiñana et al. (1994). Ulmer et al. (1994) presented the first findings from the Oriented Scintillation Spectrometer Experiment OSSE (50 keV–10 MeV), and in a CGRO-paper (Ulmer et al. 1995) the first results from OSSE, COMPTEL and EGRET were combined. It was shown that the overall pulse phase-averaged spectrum is not well fitted by a single power-law, better with a broken power-law. Phase-resolved spectra were produced and fitted with broken power laws, selecting three phase intervals (peak 1, the bridge and peak 2).

In this paper the final COMPTEL 0.75–30 MeV results on the Crab pulsar/nebula are presented using i) data from all available COMPTEL Crab observations, ii) upgraded/improved response estimates and iii) improved data selection criteria. In order to obtain a broad high-energy picture, we also consistently analysed in detail Crab data from the Italian/Dutch BeppoSAX satellite at lower energies (0.1–300 keV) and from EGRET at higher energies (30 MeV–10 GeV). For some parts of the work we analysed additional data (e.g. soft γ-ray/X-ray data from the CGRO Burst and Transient Source Experiment, BATSE, and the ROSAT HRI; and for comparisons optical and UV data).

2. Instrument description and observations

COMPTEL is the imaging Compton Telescope aboard CGRO and operates in the 0.75–30 MeV energy range. Its detection principle relies on a two layer interaction: a Compton scatter in one of the 7 upper-detector (D1) modules followed by a second interaction in one of the 14 lower-detector (D2) modules. Main measured quantities are the angles (χ, ψ) specifying the direction of the scattered photon (from the interaction loci in D1 and D2) and the energy deposits in the D1/D2 modules where the interactions took place. From the last two quantities we can calculate the scatter angle $\overline{\varphi}$ and the total energy deposit E_{tot} (for a full description see Schönfelder et al. 1993). Its energy resolution is 5–10% *FWHM* and, due to its large field of view of typically 1 steradian, it is possible to monitor a large part of the sky simultaneously with a position determination accuracy of $\sim1°$. The events are time tagged with an accuracy of 0.125 ms and are converted to Coordinated Universal Time (UTC) with an absolute accuracy better than 100 μs using the on board master clock, serving also the other 3 CGRO instruments BATSE, OSSE and EGRET.

In this study we selected all CGRO viewing periods for which the angle between the pointing axis (co-aligned with the COMPTEL/EGRET z-axis) and the Crab pulsar is less than 30°. Details for each individual observation can be found in Table 1, which is self-explanatory.

Table 1. COMPTEL observation summary with PSR B0531+21 within 30° from the pointing axis.

VP #	Start Date TJD[†]	End Date TJD	Off angle (°)	Exposure (1–3 MeV; 10^6 cm^2 s)
Cycle 0				
0.3	8374.853	8377.686	8.98	⊤
0.4	8377.894	8380.678	8.98	8.677
0.5	8380.886	8383.662	0.13	⊥
Cycle I				
1	8392.903	8406.785	6.51	10.725
31	8784.730	8798.554	27.78	9.614
36.0	8845.170	8846.765	15.55	⊤
36.5	8846.806	8854.644	16.64	12.802
39	8866.263	8882.637	17.52	⊥
Cycle II				
213	9069.778	9075.544	3.19	2.764
221	9120.708	9131.637	3.00	4.615
Cycle III				
310	9322.653	9334.635	14.59	6.387
321.1/5	9391.663	9400.636	4.49	7.622
337	9573.925	9593.594	21.38	11.143
Cycle IV				
412	9776.688	9783.672	6.48	4.307
413	9783.690	9797.589	7.54	9.161
419.1	9811.629	9818.586	25.92	4.071
419.5	9846.614	9860.634	29.17	6.221
420	9860.654	9874.688	18.28	9.462
426	9937.618	9951.581	0.13	9.629
Cycle V				
502	10007.590	10021.594	8.38	10.877
520	10210.681	10224.556	24.18	8.310
523	10259.621	10273.551	26.70	7.462
526/527/528	10294.630	10322.616	5.04[‡]	20.969
Cycle VI				
616.1	10497.670	10525.647	8.56	20.046
Cycle VII				
724.5	11001.609	11015.620	9.60	9.852
Cycle VIII				
816	11309.621	11323.581	14.59	8.132
829	11435.584	11449.597	3.00	10.826
Cycle IX				
903.1	11533.662	11540.639	16.78	4.212
918.5	11659.637	11673.620	4.00	10.543
919.5	11673.644	11690.999	19.76	9.274

[†] TJD = JD − 2440000.5 = MJD − 40000.
[‡] Weighted mean of 3 observations.

Because we have also included extensively archival EGRET data in the current study, a brief summary of this CGRO instrument is given as well. EGRET has a (gas-filled) sparkchamber and is sensitive to γ-rays with energies in the range 30 MeV to 30 GeV. In the mode used for most of the observations the field of view is approximately 80° in diameter. Its effective area is approximately 1500 cm^2 between 200 and 1000 MeV. The angular resolution is strongly energy dependent: the 67% confinement angles at 35 MeV, 500 MeV and 3 GeV are 10°.9, 1°.9 and 0°.5 respectively. The energy resolution $\Delta E/E$ is ~20% (*FWHM*) over the central part of the energy range. The relative timing accuracy is 8 μs and the absolute accuracy is better than 100 μs. For a detailed overview of the EGRET detection principle and instrument characteristics, see Thompson et al. (1993).

The X-ray data most extensively used in this work had been collected with the 4 narrow field instruments aboard BeppoSAX: the low-energy (0.1–10 keV) and medium energy (1.6–10 keV) concentrator spectrometers, LECS and MECS respectively, the High-Pressure Gas Scintillation Proportional Counter, HPGSPC (4–60 keV) and the Phoswich Detector System PDS sensitive in the 15–300 keV energy range. Detailed instrument descriptions for the 4 narrow field instruments can be found in Parmar et al. (1997), Boella et al. (1997), Manzo et al. (1997) and Frontera et al. (1997) for the LECS, MECS, HPGSPC and PDS respectively.

3. Timing analysis

The first step in the timing analysis is to subject the events registered during an observation to an event selection filter. In the case of COMPTEL the most important selection parameters are the time-of-flight TOF, the pulse shape discriminator PSD (see e.g. Schönfelder et al. 1993), the "spatial" parameters $\chi, \psi, \overline{\varphi}$ and the total energy deposit $E_{\rm tot}$. Given the a priori known position of the Crab pulsar it is possible to determine for each event the so-called $\varphi_{\rm geo}$ angle, i.e the angle between the scattered photon and the source. The $\overline{\varphi}$ angle provides an equivalent measure of this angle, but now only based on the energy deposits in both detector layers. The difference angle $\varphi_{\rm arm} = \overline{\varphi} - \varphi_{\rm geo}$ is called the Angular Resolution Measure (ARM) and forms the base of the spatial response of COMPTEL and its distribution is narrowly peaked near $\varphi_{\rm arm} = 0$ with asymmetric (energy dependent) wings. The definite and significant timing signature of the Crab pulsar in the COMPTEL energy range (Much et al. 1995; Much et al. 1997) provides a very usefull tool to determine the optimum event parameter windows for celestial sources. In this study we have determined and used subsequently the optimum (total energy deposit dependent) parameter windows for the TOF and PSD. The optimum windows for the $\varphi_{\rm arm}$ angle turn out to be asymmetric around 0 and a function of total energy deposit (as expected). Finally, for the given combination of viewing periods (see Table 1) we compared the measured $\overline{\varphi}$ distribution, dominated by background photons, with the distribution expected for a point source at the Crab position. This allows for a determination of the optimum window for selection on $\overline{\varphi}$ (a function of the total energy deposit).

Events, not vetoed by any of the 4 anti-coincidence domes surrounding the COMPTEL detector layers, and having a very low probability of originating from the Earth ("Earth Horizon angle selection") and passing through our
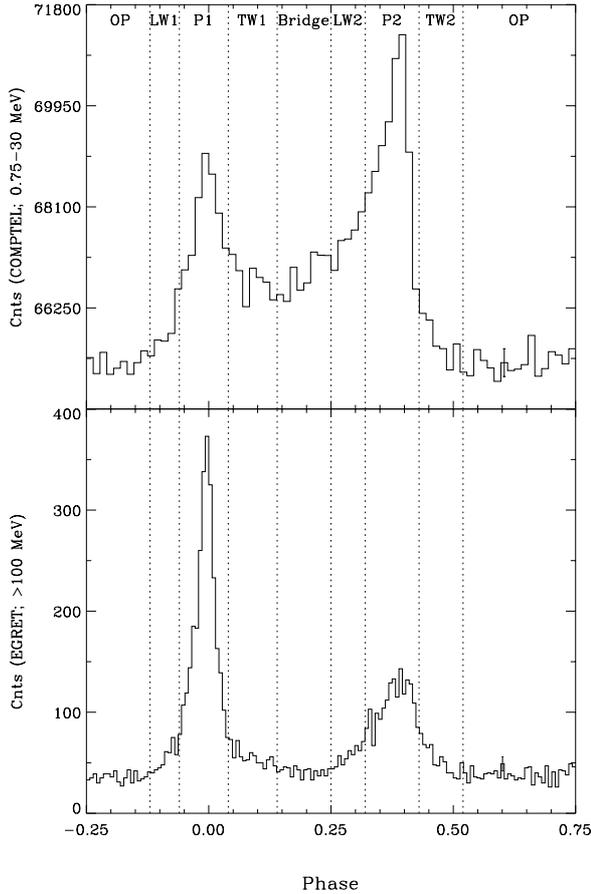
Fig. 1. Pulse profiles of PSR B0531+21 as observed by CGRO COMPTEL in the 0.75–30 MeV energy interval (top) and CGRO EGRET (bottom) for energies >100 MeV. The boundaries of the pulse phase intervals defined by Fierro et al. (1998) are indicated by the dotted vertical lines. Notice the morphology change: at energies between 0.75–30 MeV the second peak dominates, while at energies above 100 MeV the first peak dominates. Moreover, in the 0.75–30 MeV interval there is considerable bridge emission in between the two peaks, which is hardly present at energies above 100 MeV.

Table 2. Phase component definitions for the Crab pulsar adopted in this study (see also Fig. 1).

Component	Abbreviation	Phase interval	Width
Leading Wing 1	LW1	0.88–0.94	0.06
Peak 1	P1	0.94–1.04	0.10
Trailing Wing 1	TW1	0.04–0.14	0.10
Bridge	Bridge	0.14–0.25	0.11
Leading Wing 2	LW2	0.25–0.32	0.07
Peak 2	P2	0.32–0.43	0.11
Trailing Wing 2	TW2	0.43–0.52	0.09
Off Pulse	OP	0.52–0.88	0.36
Total Pulse	TP	0.88–1.52	0.64

optimized event selection windows are finally used in the timing analysis.

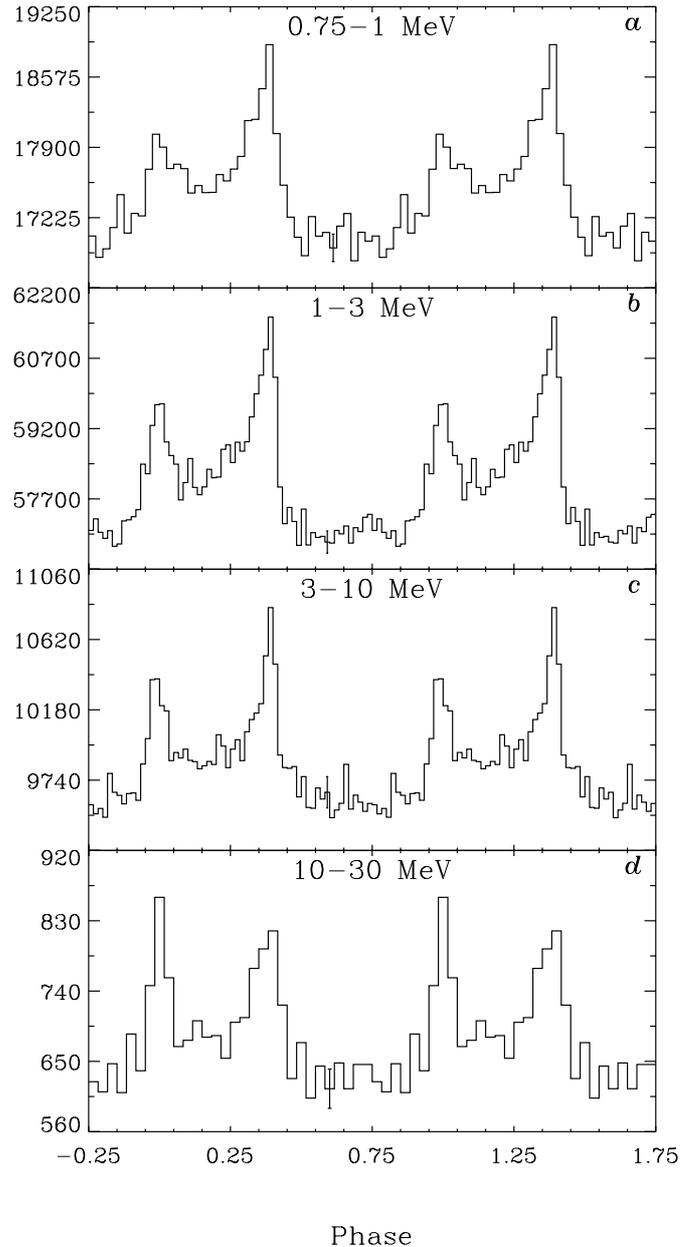The event arrival times (at the spacecraft) of these accepted events are converted to arrival times at the

Fig. 2. Pulse profiles (double cycles) of PSR B0531+21 as measured by CGRO COMPTEL in 4 differential energy intervals: 0.75–1, 1–3, 3–10 and 10–30 MeV. Typical error bars are shown near phase 0.6. A clear morphology change of the pulse profiles is visible: below 10 MeV the second peak (near phase 0.4) dominates, and emission in the "bridge" phase interval is significant, while above 10 MeV the first peak (near phase 0.0) dominates with strongly reduced "bridge" emission.

barycentre of the solar system (SSB) using the JPL DE200 solar system ephemeris and the Crab pulsar position. This process yields SSB arrival times with an absolute timing accuracy of less than 100 μs. Subsequent phase folding using the Crab pulsar ephemeris data (CGRO timing database; Arzoumanian 1992) yields the pulse profile. Because the Crab pulsar shows a lot of timing noise (young pulsar) the ephemerides have only a limited validity interval. Therefore, in the phase folding process we used

different timing solutions (ephemerides) for (almost) each observation given in Table 1.

The derived final – combining all observations given in Table 1 – COMPTEL pulse profile over the total energy range 0.75–30 MeV is shown in Fig. 1. The two expected peaks, separated ∼0.4 in phase, with intense emission between the peaks (bridge emission) are visible with high statistics. The total exposure has increased by a factor ∼5 compared to the last published total COMPTEL profile of the Crab (Much et al. 1995). For comparison we also show in Fig. 1 the CGRO EGRET profile for energies above 100 MeV for which we analyzed archival Cycle 0 to VI EGRET viewing periods with the Crab pulsar within 35° from the pointing axis, and in which the spark chamber was switched on. The same ephemerides have been used as for the COMPTEL data. The differences in morphology between the COMPTEL and EGRET profiles are evident. Following Fierro (1995) we used the EGRET profile shape to select narrow phase intervals for phase resolved spectroscopy studies (see below). The intervals are shown in the figure and given in Table 2. Figure 2 shows the pulse profiles (double cycles for clarity) in the 4 "standard" COMPTEL energy intervals (0.75–1, 1–3, 3–10 and 10–30 MeV). The significances applying the Z_n^2-test (Buccheri et al. 1983) with 8 harmonics on the unbinned set of pulse-phases are (expressed in Gaussian sigma's) 20.0σ, 31.7σ, 18.6σ and 10.9σ, respectively. Comparing the profiles with those presented in Much et al. (1997) shows the enormous increase in statistical quality, especially for energies above 3 MeV, due to the longer exposure in combination with our improved event selection procedures. We see the morphology change from the COMPTEL to the EGRET profile in Fig. 1 occurring over the COMPTEL energy range: below ∼10 MeV the second peak (near phase 0.4) dominates the first peak (near 0), and the bridge emission is intense, while above ∼10 MeV the first peak dominates and the bridge emission is strongly reduced.

The γ-ray profiles in Figs. 1 and 2 are time-averaged profiles, compiled over many years. Before analysing the profiles further, we first verified the long-term stability of the γ-ray signature (flux and pulse shape).

4. Long-term variability

4.1. Flux variations: Total pulsed flux in the 1–10 MeV range

We studied the time variability of the emission from the Crab pulsar by determining the "pulsed" flux in differential energy windows as a function of time. The "pulsed" flux has been derived from the number of excess counts in the Total Pulse phase interval (see Table 2) on top of the average emission level in the Off Pulse phase interval. For the latter interval we assume that the emission originates from the nebula only, although a DC-contribution from the pulsar can not be ruled out. We show as examples the 1–3 and 3–10 MeV results. These results over the more
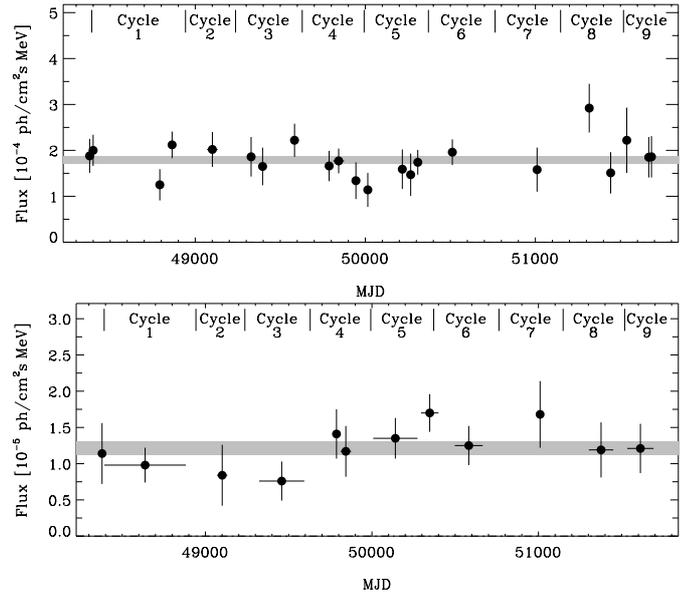

Fig. 3. "Total Pulsed" flux from the Crab pulsar as a function of time in the 1–3 MeV (top) and 3–10 MeV (bottom) energy intervals. The $\pm1\sigma$ uncertainty intervals assuming a constant flux are indicated by the shaded regions in both figures. The χ_ν^2-values for the fits assuming the flux being constant are ∼0.5, thus there is no indication for "Total Pulsed" flux variability in both the 1–3 and 3–10 MeV energy intervals.
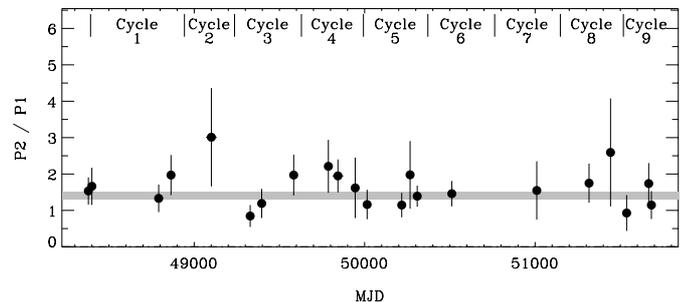

Fig. 4. The P2/P1 flux ratio of the Crab pulsar in the 1–3 MeV energy interval as a function of time. The $\pm1\sigma$ uncertainty interval assuming a constant ratio is indicated by the shaded region. The P2/P1 ratio is consistent with being constant.

than 9 year baseline (April 1991/ May 2000) are shown in Fig. 3. For the 1–3 MeV energy interval typical integration times are 2/3 weeks, while in the 3–10 MeV interval longer integration times are used given the strongly reduced statistics. The χ_ν^2 values for the fits assuming a constant flux level are typically ∼0.5 for both energy ranges, indicating that there is no evidence for time variability. Fierro (1995) also studied the Crab long-term variability for energies above 100 MeV and also concluded that the emission from the Crab pulsar is stable.

4.2. Pulse shape variations: P2/P1 ratio in the 1–3 MeV range

The time variability of the pulse shape was investigated in the 1–3 MeV (best statistics) energy window by

determining the P2/P1 ratio for each observation. This ratio is derived by measuring the number of excess counts in the P2 and P1 phase intervals (see Table 2) on top of the level in the Off Pulse interval. This ratio is shown in Fig. 4. The χ^2_ν value for a fit assuming a constant P2/P1 ratio is $\sim$0.8. Therefore, there is no indication for a time dependency of the pulse shape at medium energy γ-ray energies consistent with the findings presented by Carramiñana et al. (1994). For energies above 30 MeV Fierro (1995) studied the long-term temporal variation of the P2/P1 ratio and found also no evidence for a (systematic) variation over the Cycle 0-III EGRET observations. Tompkins et al. (1997) came to a similar conclusion using an extended EGRET data base including also Cycle IV–V.

5. Pulse profiles of PSR B0531+21 from 0.1 keV up to 10 GeV

The γ-ray pulse profiles in Fig. 2 show that the pulse morphology changes significantly over the COMPTEL energy window (0.75–30 MeV), i.e. the emission spectra vary significantly with phase. Phase-resolved spectral analyses have earlier been performed at X-ray and γ-ray energies for different data sets and/or different narrow energy intervals. However, for each study, different phase selections have been made such that a consistent full high-energy picture of the Crab pulsar can not be compiled from published results. Therefore, we extended our energy window by analysing *consistently* not only the CGRO EGRET (30 MeV–10 GeV) high-energy γ-ray data, but also X-ray/soft γ-ray data from the ROSAT HRI (0.1–2.4 keV), BeppoSAX LECS (0.1–10 keV), MECS (1.6–10 keV) and PDS (15–300 keV), and CGRO BATSE (20 keV–1 MeV).

The (on board folded) data from CGRO BATSE overlap in energy with the data from CGRO OSSE for which results have already been published by Ulmer et al. (1994, 1995). However, due to the enormous exposure in the co-added BATSE data the statistics are much better than can be obtained in the combined OSSE Crab observations. Especially above $\sim$220 keV (e.g. Ulmer et al. 1994, Fig. 2) where the OSSE data have low statistical quality, the BATSE profiles are superior. For the high statistics OSSE data (below $\sim$220 keV) we verified that the profiles are consistent in shape with those obtained by us using BeppoSAX PDS and CGRO BATSE data.

In the next subsections details are given about the compilation of Crab pulse profiles over the energy range 0.1 keV to 10 GeV.

5.1. ROSAT HRI 0.1–2.4 keV pulse profile

The soft X-ray ROSAT HRI data were collected during an observation of the Crab pulsar/nebula performed from 4 March 1995 to 15 March 1995 yielding a net exposure time of 7.98 ks (*HEASARC* Online Service; observation identifier *RH400639N00*). Because the data are spread over 115 different orbital intervals over the 11 day observation period the considerable ROSAT clock drift will
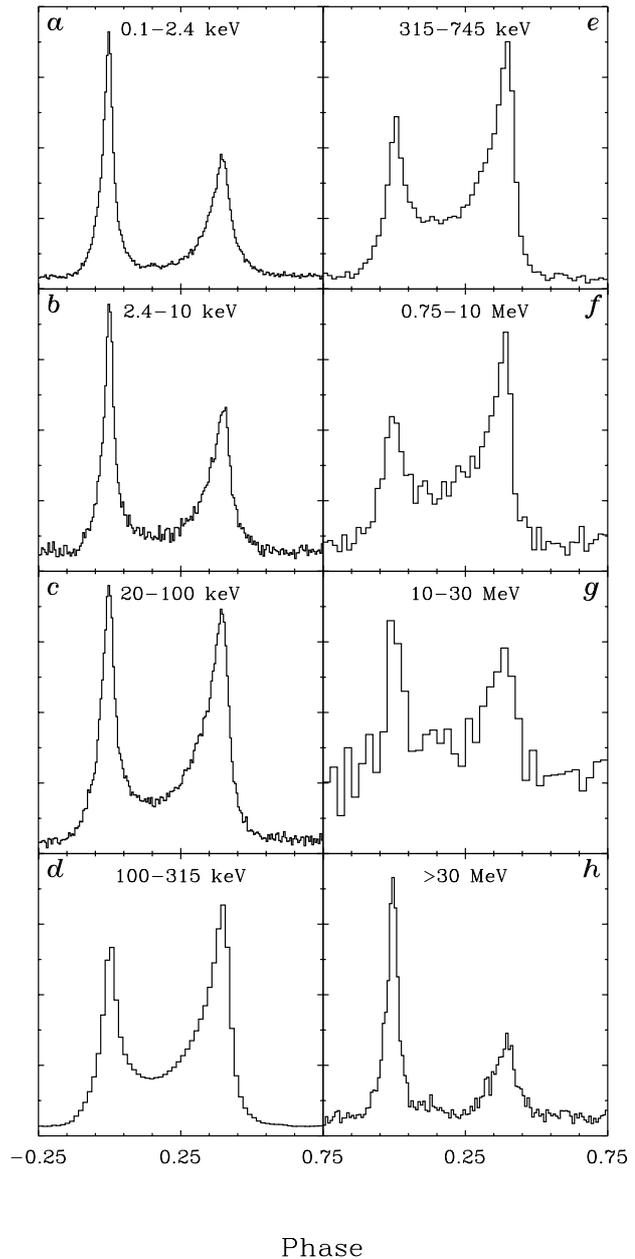
Phase

Fig. 5. High-energy pulse profiles of PSR B0531+21 from 0.1 keV up to 10 GeV. Data have been used from the following instruments: **a)** ROSAT HRI (0.1–2.4 keV), **b)** BeppoSAX MECS (2.4–10 keV), **c)** BeppoSAX PDS (20–100 keV), **d), e)** CGRO BATSE (100–315 keV & 315–750 keV), **f), g)** CGRO COMPTEL (0.75–10 MeV & 10–30 MeV) and **h)** CGRO EGRET (>30 MeV). The morphology change of the profiles as a function of energy is striking.

result in a messy pattern when combining the pulse phases from the entire observation. We could identify 4 consecutive sets of orbital intervals in which the observed pulse profile is stable. The 0.1–2.4 keV pulse profile shown in Fig. 5a was obtained cross-correlating 3 of the 4 profiles with the profile chosen as template, correcting for the observed mutual phase shifts and fixing the zero phase at the centre of the main peak.

5.2. BeppoSAX 2.4–100 keV pulse profiles

The BeppoSAX LECS, MECS and PDS data have been collected during a calibration observation of the Narrow Field instruments aboard BeppoSAX performed on 25–26 September 1999 yielding (screened) effective exposure times of 7.75 ks, 32.6 ks and 30.7 ks for the LECS, MECS (unit-2) and PDS clusters A & B, respectively (data retrieved from archive maintained by BeppoSAX ASI Science Data Center at http://www.asdc.asi.it/bepposax/; Observation Codes 20795007 & 207950071). In Figs. 5b and c the Crab pulse profiles are shown as observed by the MECS in the 2.4–10 keV energy window and by the PDS in the 20–100 keV energy window, respectively.

5.3. CGRO BATSE 100–745 keV pulse profiles

In the hard X-ray/soft γ-ray band (0.05–1 MeV) we have used archival data from the CGRO BATSE Large Area Detectors collected during observations performed between MJD 48392 and 50273 in the onboard folding mode (CGRO Archive maintained by *HEASARC* at ftp://cossc.gsfc.nasa.gov/compton/data directory batse/pulsar/onboard_folded/crab/). Typical integration times were 2/3 weeks per included observation (64 observations have been used in this study). The profiles had been produced in 64 bins per cycle in 16 different energy channels for each individual observation run. We determined the shifts of the pulse profiles of the individual observation runs with respect to the profile obtained during the observation run 48392–48406 in channel 9 (∼165–230 keV) by cross-correlation. Applying the shifts in the combination of the pulse profiles and putting the first peak at phase 0 yields high quality pulse profiles in the 20 keV–2 MeV range. In Figs. 5d and e the profiles are shown for the 100–315 keV (channels 7–10) and 315–745 keV (channels 11–13) energy windows, respectively.

5.4. CGRO COMPTEL/EGRET pulse profiles

At medium energy γ-rays the CGRO COMPTEL pulse profiles derived in this work are shown for the 0.75–10 and 10–30 MeV energy windows in Figs. 5f and g, respectively. Note that the COMPTEL profiles have a large non-zero offset. Finally, in Fig. 5h the CGRO EGRET pulse profile is given for energies above 30 MeV (we used data from Cycle 0–VI observations, retrieved from the CGRO Archive maintained by *HEASARC*; ftp://cossc.gsfc.nasa.gov/compton/data/egret/high_level/).

6. P2/P1 and Bridge/P1 ratios as a function of energy

From the (high-energy) pulse profile compilation shown in Fig. 5 we can immediately observe some striking features. The second peak (near phase 0.4) becomes more
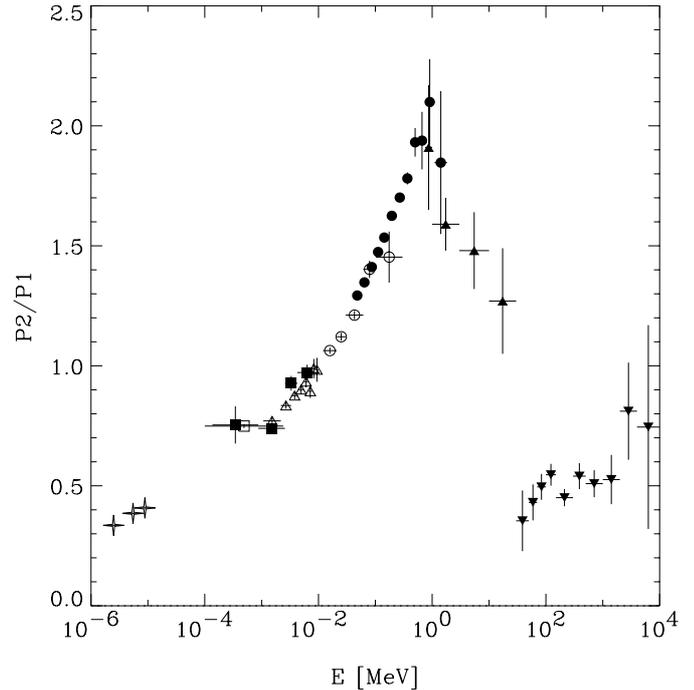

Fig. 6. P2/P1 ratio as a function of energy from optical wavelengths up to high-energy γ-rays. Data from the following instruments have been used: optical wavelengths, UCL MIC detector (star symbol), NUV/FUV HST STIS (star symbols); X-ray energies, ROSAT HRI (open square), BSAX LECS (filled square), BSAX MECS (open triangle); Hard X-rays/soft γ-rays, BSAX PDS (open circles), CGRO BATSE (filled circles); Medium/hard γ-ray energies, CGRO COMPTEL (filled upwards pointing triangle), CGRO EGRET (filled downwards pointing triangle). The gradual increase of the P2/P1 ratio up to ∼1 MeV is striking, a sharp decline in the 1–30 MeV energy range follows and a recovery to the optical ratio value settles above ∼30 MeV.

and more pronounced for increasing energies. However, above ∼10 MeV the first peak becomes dominant again. The "Bridge" emission seems to show a similar behaviour as the second peak. In a more quantitative evaluation of this morphology change of the profile as a function of energy we determined the intensity ratios for P2/P1 and Bridge/P1 as a function of energy over the entire range 0.1 keV to 10 GeV, adopting the phase interval definitions of Table 2. The pulsed emission in each interval has been separated from the underlying nebula/DC emission by subtracting the (properly scaled) emission from the OP phase interval. The results are visualized in Figs. 6 and 7 for the P2/P1 and Bridge/P1 ratios, respectively. In these plots we have also included the ratios derived from the optical profile in the 3800 to 6500 Å wavelength interval obtained by Much et al. (2000) using the UCL MIC detector as well as those in the far-ultraviolet (1140–1720 Å) and near-ultraviolet (1600–3200 Å), obtained from (time-tagged) data taken by the HST STIS instrument (Sollerman et al. 2000; Gull et al. 1998). In all optical ranges we again applied the consistent phase interval definitions.
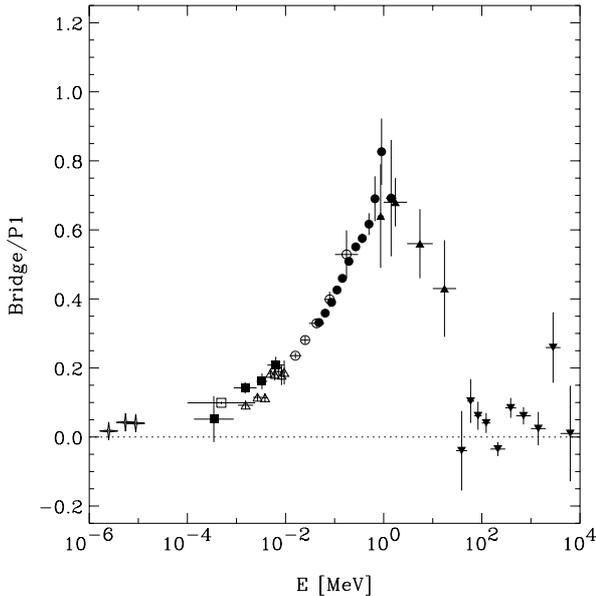
Fig. 7. Bridge/P1 ratio as a function of energy from optical wavelengths up to high-energy γ-rays. See the caption of Fig. 6 for the meaning of the symbols. The Bridge/P1 ratio is almost 0 at optical wavelengths, but gradually reaches a maximum near 1 MeV, followed by a drastic break in the 1–30 MeV energy range. Above $\sim$30 MeV the Bridge/P1 ratio approaches the optical value of $\sim$0.017.

The P2/P1 ratio as a function of energy (Fig. 6) gradually increases from the optical wavelength range to $\sim$1 MeV, followed by a rapid decrease in the 1–30 MeV interval (the COMPTEL energy window) towards a more or less constant value of $\sim$0.5 for energies above 30 MeV (the EGRET energy window). The Bridge/P1 ratio vs. energy (Fig. 7) exhibits a very similar shape as for the P2/P1 ratio. However, the values of the latter ratio in the optical and high-energy γ-ray domains, become very small (0.017) indicating that the Bridge emission practically vanishes. It is only substantial in the $\sim$1 keV to $\sim$10 MeV energy window in contrast with the emissions from the 2 peaks which are always present. This behaviour suggests that we are dealing with an emission component distinct from the emission from both peaks. This hypothesis (see e.g. also Knight 1982; Hasinger 1984, 1985; Massaro et al. 2000) is further strengthened in the phase-resolved spectral analysis presented in the next section.

Similar analyses have been presented in the past by other authors (e.g. Toor & Seward 1977; Hasinger 1984, 1985; Ulmer et al. 1994; Mineo et al. 1997; Massaro et al. 1998, 2000), generally over more restricted energy windows with poorer data coverage, and/or often using data of inferior statistical quality. Particularly the "transition" region of the COMPTEL MeV window is now well covered for the first time.

7. Spectral analysis

In this section we will first present the spectra of the nebula emission and the Total Pulse emission (excess emission in Total Pulse interval; see Table 2). Then we will show the results from the phase-resolved spectral analysis for the narrow phase intervals. As for the timing analysis, we did not limit ourselves to the analysis of the COMPTEL data, but we collected data over a very wide spectral band to derive a consistent overall high-energy picture of the Crab. Combining spectra derived by different instruments, we had to assess possible systematic effects in the flux estimates and their impact on our analysis and conclusions. For this purpose, we used the nebula spectra to estimate possible inconsistencies.

7.1. Crab nebula spectrum

To determine the Crab nebula spectrum from our COMPTEL (0.75–30 MeV) Cycle 0-IX observations (see Table 1) we selected events recorded in the Off Pulse phase interval (see Table 2), assuming that any pulsar DC emission is negligible, and applied a maximum likelihood method using the spatial signature of a point source in the $(\overline{\varphi}, \varphi_{\mathrm{arm}})$ plane as a function of measured energy. This work yielded an improved spectrum for the nebula emission in the COMPTEL energy range compared to the COMPTEL Crab nebula spectrum published earlier by van der Meulen et al. (1998). In the latter work a smaller database was used, as well as preliminary response characteristics, which have since been improved upon. The newly derived COMPTEL nebula spectrum is given in Table 3. A power-law fit to the COMPTEL nebula flux points results in a photon index of 2.227 ± 0.013. In the same table also the statistical uncertainties (1σ) on the flux measurements are provided. In this context we note that COMPTEL has an overall (systematic) uncertainty on its flux estimates of the order of 10–20%.

To cover the neighbouring soft X-ray to soft γ-ray band, we derived the BeppoSAX LECS, MECS, HPGSPC and PDS nebula spectra applying the most recent (December 1999 issue for the LECS and HPGSPC and November 1998 issue for the MECS and PDS) response characteristics (sensitive area, energy redistribution matrices and spatial response). We fitted the Sep. 1999 Off Pulse Crab data from these four BeppoSAX instruments simultaneously over the full 0.1–300 keV energy range with an absorbed power-law model taking into account the mutual uncertainties in absolute flux calibrations by including in the fit three free relative normalization scale factors (MECS scale factor fixed to 1). The energy of the LECS events used in the fit was constrained to the 0.1–4 keV window. The best photon index and Hydrogen column density N_{H}, assuming solar abundances for the other elements absorbing soft X-rays, resulting from this fit are 2.145 ± 0.001 and $3.61(2) \times 10^{21}$ cm^{-2}, respectively. In Appendix A the systematic uncertainties in the derived spectral characteristics in the X-ray/soft γ-ray band are discussed in detail comparing flux estimates obtained by different high-energy instruments.

Table 3. COMPTEL spectra of the Crab nebula and pulsar (Total Pulse). Fluxes with 1σ statistical uncertainties.

Energy window [MeV]		Nebula Flux [ph/cm^2 s MeV]	Total Pulse Flux [ph/cm^2 s MeV]
0.75	1.00	(2.585 ± 0.089)E-3	(0.650 ± 0.071)E-3
1.00	1.25	(1.563 ± 0.054)E-3	(0.452 ± 0.043)E-3
1.25	1.50	(1.127 ± 0.043)E-3	(0.270 ± 0.034)E-3
1.50	2.00	(0.617 ± 0.020)E-3	(0.165 ± 0.016)E-3
2.00	2.50	(0.306 ± 0.014)E-3	(0.084 ± 0.011)E-3
2.50	3.00	(0.217 ± 0.010)E-3	(0.048 ± 0.008)E-3
3.00	4.00	(1.312 ± 0.055)E-4	(0.278 ± 0.045)E-4
4.00	6.00	(0.613 ± 0.022)E-4	(0.126 ± 0.018)E-4
6.00	8.00	(0.284 ± 0.014)E-4	(0.062 ± 0.011)E-4
8.00	10.0	(1.637 ± 0.082)E-5	(0.288 ± 0.066)E-5
10.0	15.0	(0.734 ± 0.033)E-5	(0.244 ± 0.027)E-5
15.0	30.0	(0.201 ± 0.013)E-5	(0.039 ± 0.011)E-5

For the adjacent EGRET high-energy (30–30 000 MeV) γ-ray range we derived (phase-resolved) Crab spectra using all available Cycle 0–IV archival EGRET data for which reliable sensitivity estimates were available to us[1]. The method is equivalent to the spatial maximum likelihood analysis performed by Fierro (1995). The only difference with the latter work is that we now added Cycle-IV data. The EGRET spectral data are claimed to be 10% accurate (Thompson et al. 1995).

The Crab nebula spectrum from 0.1 keV up to 50 TeV is shown in an $E^2 \times F$ representation in Fig. 8. Included are the BeppoSAX, COMPTEL and EGRET spectra derived in this work, soft γ-ray spectral information from GRIS (0.02–1 MeV; Bartlett et al. 1994a) together with ground-based TeV data (STACEE-32 > 0.19 TeV, Oser et al. 2001; HEGRA 1–20 TeV, Aharonian et al. 2000; Whipple 0.5–8 TeV, Hillas et al. 1998; CANGAROO 7–50 TeV, Tanimori et al. 1998). Similarly to the spectrum shown in van der Meulen et al. (1998), but now more pronounced, we see a continuous and smooth decrease from soft X-rays up to medium energy γ-rays, irrespective of the uncertainties in the absolute sensitivities of the instruments, followed by a steep gradient beyond $\sim$30 MeV to $\sim$300 MeV. Above $\sim$300 MeV an additional emission feature seems to emerge reaching a maximum between 10 and 100 GeV, a window which is not yet accessible for spaceborne and ground-based experiments. For an interpretation of this spectral shape, see e.g. de Jager et al. (1996).

7.2. Crab Total Pulse spectrum

In the 0.75–30 MeV energy range we determined the pulsed flux values from all CGRO COMPTEL observations (see Table 1) in two distinct manners. In the first method, the number of (pulsed) excess counts in the broad Total Pulse interval (see Table 2) above the mean level in the Off Pulse interval is determined as a function of measured energy. These excess counts are then converted to flux values using the COMPTEL response and the total exposure. The second approach is based on the maximum likelihood method in the spatial domain as introduced in Sect. 7.1. Applying the latter approach for pulse-phase selected events and subtracting the properly scaled Off Pulse contribution (containing only the DC/nebula source with a point source signature) yields the pulsed fluxes as a function of energy for the selected pulse-phase intervals. We verified for the Total Pulse interval, having the best statistics, that the fluxes derived from both methods are compatible within 5−20%, giving a measure of the systematic uncertainties. The COMPTEL Total Pulse fluxes from the spatial analysis (remember, nebula emission subtracted) are also included in Table 3 and shown in Fig. 9.

For comparison, we included in Fig. 9 our derived Total Pulse Crab EGRET spectrum (30 MeV–10 GeV, Cycle 0–IV) and the published Total Pulse spectra from GRIS (20 keV–1 MeV: Bartlett 1994a) and OSSE (50 keV–0.59 MeV: Ulmer et al. 1994). In the latter two publications slightly different phase intervals have been used to derive the Total Pulse spectrum.

In the COMPTEL Total Pulse spectrum a feature becomes apparent: the high flux value in the 10–15 MeV interval, consistently derived in both the timing and spatial methods. A response anomaly is excluded, e.g. the nebula 0.75–30 MeV spectrum (cf. Fig. 8) exhibits a very smooth behaviour over its entire range, nor has such an effect been seen in other COMPTEL analyses. Fitting the COMPTEL flux points with a power-law spectral model, excluding the deviant 10–15 MeV flux point, yields a good fit with photon index of 2.35 ± 0.06 ($\chi^2_\nu = 0.50$ for 9 d.o.f.), connecting smoothly at both ends to the GRIS/OSSE and EGRET flux measurements. The excess flux in the 10–15 MeV interval above this power-law model fit reaches a significance of 3.5σ. Including the deviant 10–15 MeV flux point in the spectral fit yields a worse fit ($\chi^2_\nu = 1.42$ for 10 d.o.f.) with a power-law index of 2.24 ± 0.04, which does not connect smoothly to the neighbouring measurements, particularly to EGRET. The 10–15 MeV excess flux above this fit has a significance of only 2.0σ. We do therefore not regard the 10–15 MeV flux enhancement as a firm detection of a new spectral feature, and have no possible astrophysical interpretation, but we find it interesting to note that contributions to this flux enhancement appear to come from those (narrow) phase intervals in which a broad spectral (Bridge) component dominates the spectrum (see Sect. 7.3). If genuine, it could therefore be related to this spectral component.

For the BeppoSAX LECS, MECS and PDS we determined the number of (pulsed) excess counts above the mean level in the Off Pulse phase interval, similarly to the first COMPTEL method. These excess counts have been converted to flux measures applying the most

---

[1] Due to the problem of gas aging, the spark chamber efficiency degraded significantly during the later Cycles of the EGRET CGRO observations. Recently, the EGRET team did present the energy and time dependent correction factors for the later Cycles (Gamma 2001 Symposium, Baltimore).
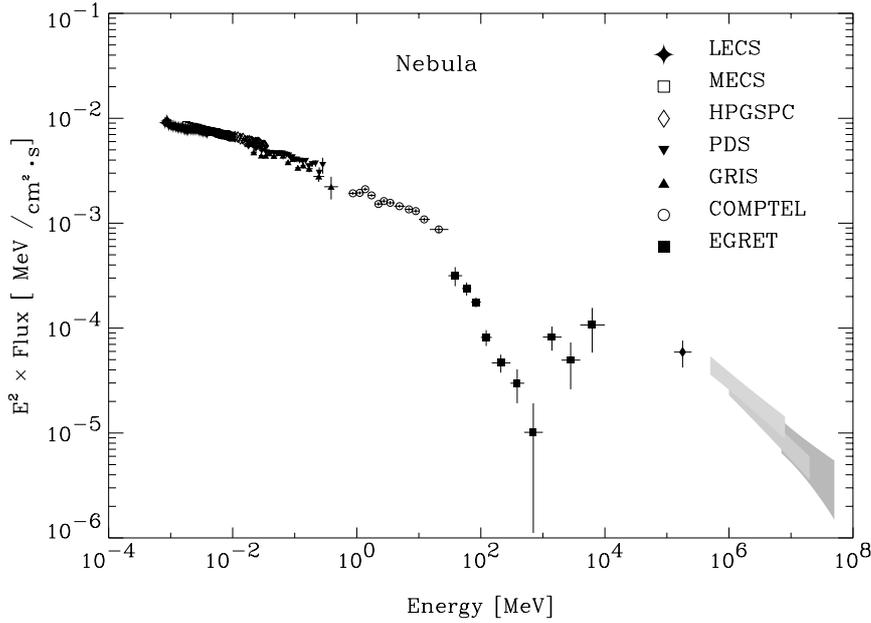
Fig. 8. The Crab nebula spectrum from soft X-rays up to TeV γ-rays. The TeV data point near 1.6×10^5 MeV is taken from Oser et al. (2001) and the hatched bands represent the flux measurements and corresponding 1σ uncertainty estimates at TeV energies (for references, see text).
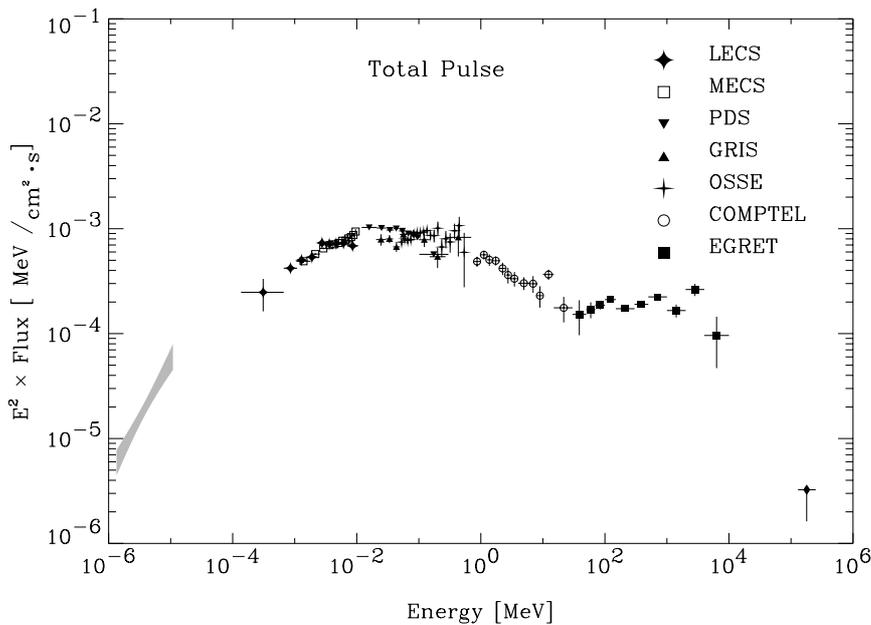

Fig. 9. The Total Pulse emission of the Crab pulsar from optical wavelengths up to high-energy γ-rays. The nebula emission has been subtracted. The optical spectral data (10^{-6}–10^{-5} MeV) are taken from Sollerman et al. (2000) and the TeV data point near 1.6×10^5 MeV from Oser et al. (2001).

recent response characteristics assuming intrinsic power-law type emission absorbed in a column of density $N_{\mathrm{H}} = 3.61(2) \times 10^{21}$ cm^{-2} (see Sect. 7.1). In this way we obtained the Total Pulse spectrum over the 0.1–300 keV energy interval, which is also shown in Fig. 9.

We augmented the energy coverage by including the pulsed spectra obtained at optical/NUV/FUV wavelengths by Sollerman et al. (2000). In this $E^2 \times F$ representation, the total pulsed emission shows a gradual increase from the optical range towards a plateau of maximum luminosity extending from $\sim$10 keV to $\sim$1 MeV. Beyond $\sim$1 MeV the emission softens until $\sim$70 MeV, above which a second plateau appears with an emission spectrum having a photon power-law index close to 2. Between 4 and 10 GeV the pulsar spectrum appears to break/soften

drastically to account for the recently derived upper limits for pulsed emission at TeV γ-ray energies (see e.g. Vacanti et al. 1991; Borione et al. 1997; Aharonian et al. 1999; Lessard et al. 2000; Oser et al. 2001). Its spectral behaviour is completely different from that of the nebula (cf. Fig. 8). Notice the dominance of the nebula emission component over the pulsed emission component for energies below $\sim$100 MeV and above $\sim$10 GeV, comparing Figs. 8 and 9. Only in a small window at high-energy γ-rays between $\sim$100 MeV and $\sim$10 GeV the pulsed component exceeds the underlying nebula component. This Total Pulse spectrum is clearly complex. For detailed theoretical interpretations it is important to disentangle first this total spectrum in contributions from different phase components of the pulse profile.
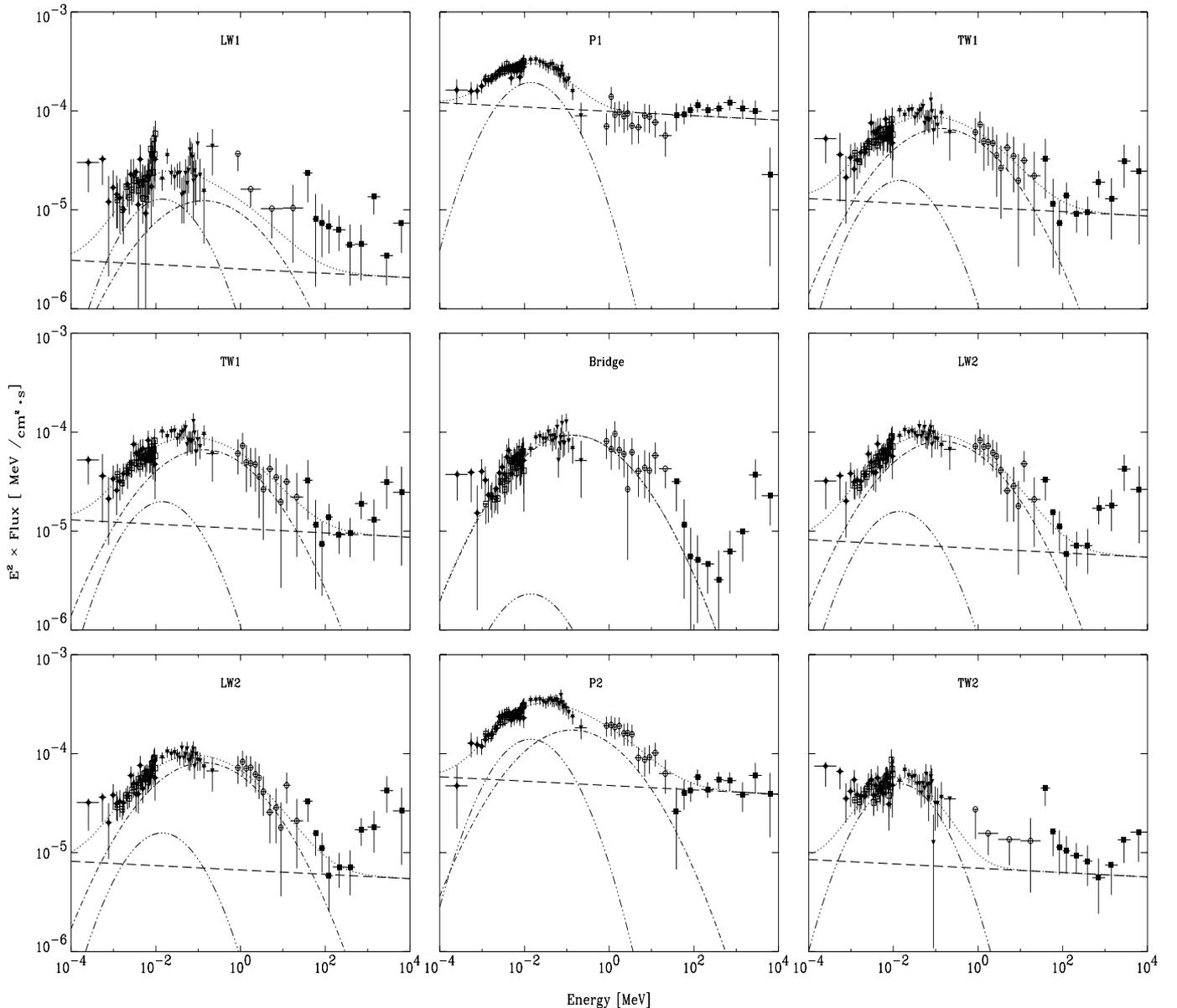
Fig. 10. The high-energy emission of the Crab pulsar in the 7 narrow pulse-phase intervals (see Table 2) from 0.1 keV up to 10 GeV. Two spectra (for the TW1 and LW2 phase intervals) are displayed twice, to facilitate a better visual comparison of the different spectra (see discussion). See Fig. 9 for the meaning of the symbols of the data points. The different contributions (P1 modified power-law model, dash-dot-dot-dot line; Bridge modified power-law model, dash-dot line; power-law model, dash line) to the composite model fits (dotted lines) have all been superimposed for the best-fit scaling parameters (histogram) shown in Fig. 11.

7.3. Spectral behaviour in the narrow pulse-phase intervals

A similar broad-band spectral analysis (0.1 keV–10 GeV), as presented in Sect. 7.2 for the Total Pulse interval, has been performed for the 7 narrow pulse-phase intervals defined within the Total Pulse phase interval (see Table 2). We analyzed data from the BeppoSAX LECS, MECS and PDS and CGRO COMPTEL and EGRET instruments applying identical phase window selections. Since we planned to make empirical fits to the multi-instrument spectra, we wished to avoid being too sensitive to the systematic discrete jumps in the overlapping spectra of the BeppoSAX LECS, MECS and PDS and GRIS, as shown in Fig. A.1. In the spectra and analysis presented here, we added a representative 10% systematic flux uncertainty to the statistical uncertainty in each flux measurement involved (for COMPTEL 15% was used). We also repeated the total analysis normalizing the BeppoSAX data on the much lower GRIS value, as well as on the average normalization value of the BeppoSAX instruments. Our results are not sensitive to these different normalizations.
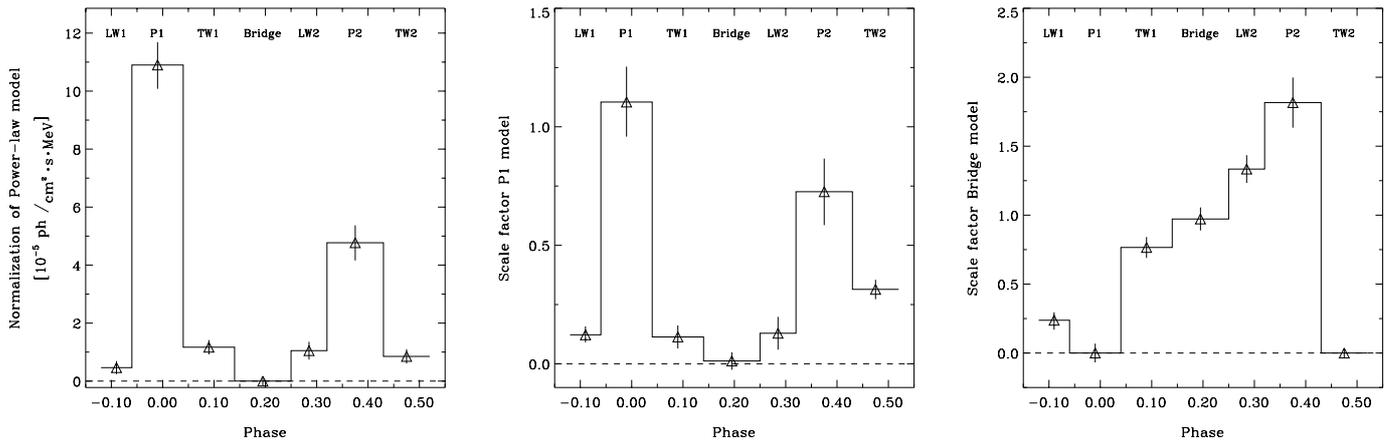
Fig. 11. Scale factors of the 3 empirical spectral models as a function of phase: left panel, power-law model scale factor; middle panel, "narrow" bump (P1 modified power-law component) scale factor; right panel, "broad" bump (Bridge modified power-law component) scale factor.

The spectral results for the seven different intervals are shown in Fig. 10[2]. This compilation clearly shows that the spectral shape varies strongly with pulsar phase. For example, the spectra of the P1 and the Bridge intervals differ dramatically. Emission from the latter is hardly discernible at energies below 1 keV and above 100 MeV; this emission is confined roughly between these energies in a broad "bump" shaped fashion in this $E^2 \times F$ representation. On the other hand, the emission in the P1 interval remains very strong in the γ-ray domain above 1 MeV (COMPTEL and EGRET data), exhibiting a power-law photon distribution up to a spectral break at GeV energies. Extrapolation of such a power-law spectral shape to X-ray energies, reveals a narrower "bump" shaped excess above the power-law extrapolation, with a maximum power output well below 50 keV. The P2 spectrum is rather similar to the spectrum of P1, but a spectral component similar in shape to that of the Bridge interval seems to enhance the P2 spectrum at MeV energies, relative to the P1 spectrum. Finally, the Trailing Wing 1 (TW1) and Leading Wing 2 (LW2) spectra are amazingly similar in shape, and appear to be some mixture of shapes of P1 and the Bridge intervals. This should not be a surprise, because the adopted separation in phase intervals (Table 2) will most likely not coincide exactly with genuine physical components (different dominating production mechanisms and/or production sites in the Crab magnetosphere). However, the vastly different spectral behaviour exhibited in the Bridge phase interval suggests a physically distinct emission component as proposed earlier by e.g. Knight (1982) and Hasinger (1985).

7.4. Parametrization of the emission in the narrow pulse-phase intervals

Exploiting our high statistics and eight-decades wide high-energy phase-resolved spectra, we made an attempt to empirically disentangle in phase and energy space underlying physical components. Assuming again that the Bridge spectrum represents the shape of a distinct emission component, we modelled its spectral behaviour in terms of two spectral components, a "modified" power-law (mpl) with an energy dependent index and a simple power-law (pl): $F = F^{\mathrm{mpl}} + F^{\mathrm{pl}} = \alpha \cdot E^{-(\beta + \gamma \cdot \ln E)} + \alpha_{\mathrm{pl}} \cdot E^{-\beta_{\mathrm{pl}}}$. In this formula F denotes the photon flux in units ph/cm^2 s MeV, while E is given in MeV. As expected, the normalization parameter α_{pl} for the simple power-law component was consistent with zero, although a weak level of high-energy γ-ray emission is measured up to GeV energies. The same approach has been followed for the emission in the P1 interval. The resulting simple power-law component, describing entirely the high-energy end of the spectrum, has an index 2.022 ± 0.014. We note that this power-law spectrum has to break near the boundaries of the energy window shown in Fig. 10 (see also Fig. 9). The resulting best fit values for the "modified" power-law components of the P1 and Bridge emissions are given in Table 4. From these values we can derive the following positions for the maxima (in the $E^2 \times F$ flux representation): 14.0 ± 1.1 keV and 135 ± 15 keV for the P1 and Bridge phase intervals, respectively. The widths of the "modified" power-law components are specified by the FWHM values in the $^{10}\log(E)$ domain and are about 1.81 and 2.65 for the P1 and Bridge intervals, respectively. With this approach we have identified three distinctly different spectral shapes, which can describe the P1 and Bridge spectra.

---

[2] The phase-resolved spectral data can be retrieved from `http://ws13.sron.nl:8080/personal/kuiper/data`

Table 4. Best fit parameter values for the "modified" power-law and power-law components of the P1 phase interval and for the "modified" power-law of Bridge phase interval.

Component	α (ph/cm^2 s MeV)	β	γ
P1-mpl	(1.06 ± 0.07)E-5	3.361 ± 0.014	0.159 ± 0.003
P1-pl	(9.98 ± 0.69)E-5	2.022 ± 0.014	
Bridge-mpl	(7.09 ± 0.51)E-5	2.298 ± 0.017	0.074 ± 0.003

In the next step we made an attempt to describe the measured spectral distributions in the narrow pulse-phase intervals (npi) in terms of just these 3 models each with a free scaling parameter: $F^{\mathrm{npi}} = a \cdot F^{\mathrm{Bridge\text{-}mpl}} + b \cdot F^{\mathrm{P1\text{-}mpl}} + c \cdot E^{-\beta_{\mathrm{P1\text{-}pl}}}$.

Interestingly, the resulting fits are very satisfactory for all phase intervals as shown in Fig. 10 in which the composite model (dotted lines) and the individual components are superimposed on the measured spectra. The fit characteristics for each phase interval are shown in Table 5. The χ^2_ν values of the fits indicate acceptable spectral descriptions in all cases. The inclusion of 10–15% systematic uncertainties in the flux measurements, however, makes a straightforward assessment/interpretation of the χ^2_ν values difficult.

In Table 5 two types of error estimates are presented for each scaling parameter. The first type is associated with the (asymmetric) statistical uncertainty in the scale parameter using the best fit estimates for the parameters describing the shape of the 3 models i.e. $\beta_{\mathrm{P1\text{-}mpl}}$, $\gamma_{\mathrm{P1\text{-}mpl}}$, $\beta_{\mathrm{Bridge\text{-}mpl}}$, $\gamma_{\mathrm{Bridge\text{-}mpl}}$ and $\beta_{\mathrm{P1\text{-}pl}}$ (see Table 4). The second type is related to the systematic uncertainty in the fitted scale parameter and has been determined by varying the shape parameters of the 3 models within their $\pm 1\sigma$ errors. The range over which the scale parameters vary is indicative for the systematic uncertainty due to uncertainties in the shape of the 3 model fit functions.

The fit results for the 3 scale parameters are visualized in Fig. 11. These scale parameters have been normalized to the emission in the Bridge interval because of the different phase extents of the intervals. Figure 11 shows effectively the "light curves" of these model components: two components are clearly related to the emission in the two main pulses (the power-law component and the "narrow bump") and the "Bridge component" or "broad bump" extends apparently from the LW1 till under P2 in a triangular shape.

The "light curves" in Fig. 11 can also be clearly discerned in the 9 panels of Fig. 10. The upper row centered on P1 shows how the components of P1 extend into the wings; the middle row shows how the Bridge spectrum dominates in all three intervals and how the power-law component and the "narrow bump" contributions are symmetrically distributed on either side of the Bridge interval. Finally, the lowest row centered on P2 looks very

much like the upper row, but the Bridge spectral component reaches a maximum value in P2. We have apparently succeeded in identifying likely genuine underlying physical components in phase and energy space.

7.5. Enhanced high-energy γ-ray emission in the LW2 interval

The most apparent and significant (4.3σ for energies above 300 MeV) deviation from the composite fits in Fig. 10 is visible in the LW2 spectrum in the EGRET range above 100 MeV. Fierro (1995) reported for this phase interval the hardest pulsed γ-ray spectrum (photon index 1.69 ± 0.08) fitting CGRO Cycles 0–III EGRET data. For our (timing) analysis we used CGRO Cycle 0–VI EGRET data, almost doubling the statistics for energies above 1 GeV[3].

To verify whether the phase distributions in the GeV energy range also show evidence for a separate hard *spectral* component in front of P2 we produced the pulse profiles of Fig. 12: the 1–10 GeV pulse profile superimposed on the 100–300 MeV profile for EGRET Cycle 0–VI observations. The two distributions are normalized on the P1 phase interval. A clear increase of emission in the LW2 phase interval (0.25–0.32) is visible for the highest energies, but the enhancement seems to extend to the maximum in the P2 phase interval, however constituting a minor fraction in the latter. The effect can be interpreted as a phase shift of the second pulse with increasing energy, but also as a "new" spectral component (phases $\sim$0.2–0.4) with respect to the composite fits with three spectral components as shown in Fig. 10. Ramanamurthy (1994) and Eikenberry & Fazio (1997) discussed variations in the intra-peak phase separations as a function of energy. A further phase shift above 1 GeV is consistent with the reported trend.

Considering the enhancement a new spectral component then its spectrum must be even harder than derived by Fierro (1995). Fitting for the LW2 phase interval another power-law model with both a free normalization and a free index on top of the model composed of the broad and narrow spectral components and the power-law component with a fixed index of 2.022, we find for the additional power-law model a very hard photon index of $1.44^{+0.05}_{-0.04}$. However, our data are not of sufficient quality to discriminate between an additional very hard power-law component, which must break somewhere above 10 GeV to be consistent with the non-detections of pulsed emission at TeV energies, or for example an additional high-energy "bump". This can be studied in detail with the next generation high-energy γ-ray telescopes AGILE and particularly GLAST (see e.g. `http://glast.gsfc.nasa.gov`), which is $\sim$30 times more sensitive than EGRET over a much wider energy interval extending to 300 GeV.

---

[3] For energies lower than 1 GeV the increase in statistics is less due to the energy and time dependent EGRET sensitivity caused by spark-chamber gas aging.

Table 5. Best fit scale factors (a, b, c) for the narrow phase intervals.

Interval	a	b	c	χ^2_ν ($\chi^2/n_{\text{d.o.f.}}$)
LW1	$0.130^{+0.024}_{-0.029}\,{}^{+0.008}_{-0.008}$	$0.067^{+0.011}_{-0.009}\,{}^{+0.008}_{-0.008}$	$(\ 2.53^{+1.01}_{-1.00}\,{}^{+0.22}_{-0.22})$E-6	$0.94\ (69.83/(77-3))$
P1	$0.000^{+0.061}_{-0.061}\,{}^{+0.001}_{-0.001}$	$1.004^{+0.050}_{-0.047}\,{}^{+0.086}_{-0.086}$	$(99.09^{+4.59}_{-4.93}\,{}^{+2.52}_{-2.52})$E-6	$0.66\ (53.80/(85-3))$
TW1	$0.696^{+0.052}_{-0.052}\,{}^{+0.017}_{-0.017}$	$0.103^{+0.019}_{-0.019}\,{}^{+0.025}_{-0.025}$	$(10.62^{+1.85}_{-1.86}\,{}^{+0.39}_{-0.39})$E-6	$0.46\ (38.07/(85-3))$
Bridge	$0.972^{+0.051}_{-0.050}\,{}^{+0.033}_{-0.033}$	$0.012^{+0.018}_{-0.018}\,{}^{+0.019}_{-0.019}$	$(\ 0.01^{+1.40}_{-1.41}\,{}^{+0.07}_{-0.07})$E-6	$0.76\ (62.48/(85-3))$
LW2	$0.849^{+0.048}_{-0.048}\,{}^{+0.016}_{-0.016}$	$0.082^{+0.017}_{-0.017}\,{}^{+0.027}_{-0.027}$	$(\ 6.68^{+1.59}_{-1.60}\,{}^{+0.35}_{-0.35})$E-6	$0.59\ (48.22/(85-3))$
P2	$1.816^{+0.118}_{-0.122}\,{}^{+0.064}_{-0.064}$	$0.726^{+0.047}_{-0.048}\,{}^{+0.093}_{-0.093}$	$(47.71^{+4.05}_{-4.15}\,{}^{+1.95}_{-1.95})$E-6	$0.48\ (39.61/(85-3))$
TW2	$0.000^{+0.027}_{-0.027}\,{}^{+0.000}_{-0.000}$	$0.257^{+0.016}_{-0.017}\,{}^{+0.017}_{-0.017}$	$(\ 6.96^{+1.53}_{-1.53}\,{}^{+0.48}_{-0.48})$E-6	$0.83\ (61.10/(77-3))$
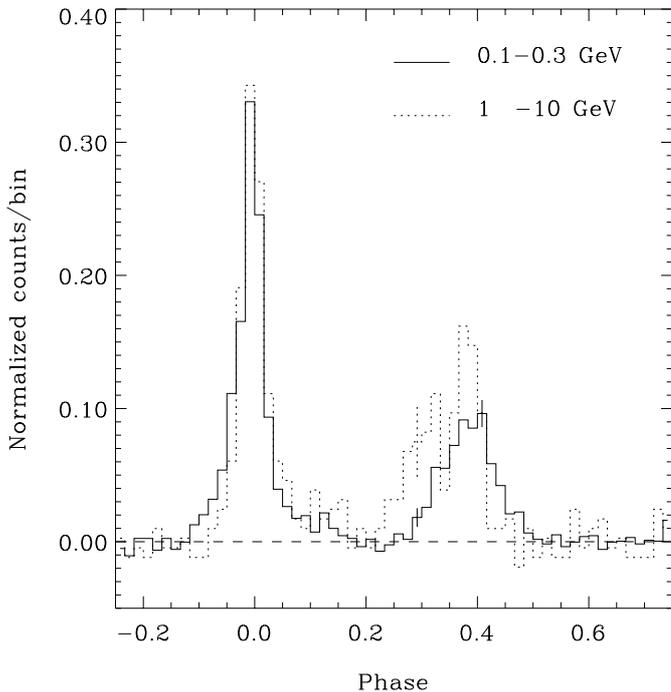
Fig. 12. EGRET pulse profiles (60 bins) using CGRO EGRET Cycle 0–VI data: 1–10 GeV, dotted line; 100–300 MeV, solid line. The profiles are normalized on their emission in P1. Typical error bars are indicated for both profiles. A clear increase is visible in the LW2 phase interval (0.25–0.32) for the 1–10 GeV energy interval with respect to the 100–300 MeV interval.

8. Summary and discussion

In this work we derived final COMPTEL pulse profiles and spectra for the Crab pulsar and nebula at medium γ-ray energies (0.75–30 MeV) using data collected over the 9 year mission of NASA's Compton Gamma-Ray Observatory.

Due to the high counting statistics over the total 0.75–30 MeV interval, we were able to show a clear morphology change of the pulse profile as a function of energy, providing clear evidence for drastic spectral variations with pulsar phase over the COMPTEL energy window. Indications for such variations were found in the earlier COMPTEL analysis by Much et al. (1995).

Using our large COMPTEL data base we derived an improved Crab nebula spectrum, which has a power-law spectral shape between 0.75 and 30 MeV with index 2.227 ± 0.013. Also our new COMPTEL spectrum for the total pulsed emission (nebula/DC emission subtracted) can be described with a power-law spectral shape between 0.75 and 30 MeV with index 2.24 ± 0.04. If the indication for enhanced emission in the 10–15 MeV interval is genuine, then the index becomes, 2.35 ± 0.06.

These improved COMPTEL findings have been put in a much broader context by including in our analysis data from instruments sensitive at the neighbouring X-ray/soft γ-ray energies, particularly from the BeppoSAX LECS, MECS and PDS instruments, and at high γ-ray energies from CGRO EGRET.

We compiled a new spectrum of the Crab pulsed emission from optical wavelengths up to the high-energy γ-rays at 10 GeV (Fig. 9). This emission reaches a level of maximum luminosity per decade in energy from $\sim$5 keV to 50 keV. Beyond this maximum a gradual softening sets in reaching a plateau (photon power-law index of $\sim$2) near $\sim$30 MeV which continues to $\sim$10 GeV. Above $\sim$10 GeV the spectrum must break rapidly in order to be consistent with the stringent TeV upper limits for pulsed emission.

Phase resolved spectral analysis can provide important constraints for pulsar modelling, particularly to help identifying different production mechanisms and sites in the pulsars magnetosphere. Therefore, we derived consistently over a broad energy range from 0.1 keV up to 10 GeV (BeppoSAX LECS, MECS, PDS, CGRO COMPTEL and EGRET) for seven narrow phase intervals phase-resolved spectra. These spectra exhibited very different spectral shapes, most notably the spectra for the narrow Bridge and Peak 1 intervals. We could disentangle the pulsed emission in energy and phase space, exploiting the vastly different spectral shapes, particularly over the COMPTEL energy window, by making empirical fits, and found that the pulsed emission can be described with 3 distinctly different spectral components:

–1 a power-law emission component from $\sim$1 keV to $\sim$5 GeV, photon index 2.022 ± 0.014, which is present in the phase intervals of the two pulses;

–2 a curved spectral component required to describe soft (≤ 100 keV) excess emission present in the same pulse-phase intervals;

–3 a broad curved spectral component reflecting the bridge emission from 0.1 keV to ~ 10 MeV. This broad spectral component extends in phase over the full pulse profile in an approximately triangular shape, peaking under the second pulse.

Furthermore, in addition to the 3 spectral components the Leading Wing 2 (LW2) phase interval exhibited a very hard spectral component, most notably at GeV energies, which likely extends over the broader phase interval ~ 0.2–0.4.

In a somewhat different approach and using only BeppoSAX data between 0.1 and 300 keV, Massaro et al. (2000) identified recently two components: the first is the combination of the two components as described above under 1 and 2 and the second corresponds to the one described under 3. In their narrower energy window differences in spectral shapes can be well approximated by variations in power-law index.

Since the discovery of γ-ray emission from radio pulsars in the early seventies, the most popular and competing models attempting to explain the high-energy radiation from highly magnetized rotating neutron stars can be divided in two distinct catagories: the so-called Polar Cap (PC) models and Outer Gap (OG) models.

Detailed information on the PC models can be found in e.g.: Daugherty & Harding (1982, 1994, 1996), Sturner & Dermer (1994) and most recently Zhang & Harding (2000). PC models have problems in explaining the overall measured Crab pulsar characteristics. Most notably, the large angles of $\sim 60°$ estimated for both the magnetic inclination α and the viewing angle ζ, the angle between the spin axis and the observer's line of sight, from radio and optical/UV observations cannot be reconciled (see for recent publications e.g. Graham-Smith et al. 1996; Moffett & Hankins 1999; Everett & Weisberg 2001).

OG models have no difficulties with the large α and ζ angles estimated for the Crab, as is clearly shown by Chiang & Romani (1994). In these models the acceleration of charged particles and production of high-energy radiation takes place in charge depleted gaps between the null-charge surface, defined by $\boldsymbol{\Omega} \cdot \boldsymbol{B} = 0$ with $\boldsymbol{B}$ the local magnetic field, and the light cylinder (with radius $R_{\mathrm{lc}} = c/\Omega$) above the last closed field lines. For early papers and later refinements see: Cheng et al. (1986a, b), Ho (1989), Chiang & Romani (1994), Romani & Yadigaroglu (1995), Romani (1996) and Yadigaroglu (1997). Recently, Cheng et al. (2000) presented a three-dimensional outer gap model building on the work of Romani and co-workers. The emission patterns from these outer gap models resemble fan beams, and double peak profiles with (strong) bridge emission can commonly be generated for the cases that emission is seen from only one pole, e.g. Romani (1996), as well as from both poles, Cheng et al. (2000).

Early attempts to model the Crab Total Pulse spectrum in an OG scenario using various radiative processes like the curvature, synchrotron and inverse Compton radiation mechanisms, assumed to play a key role in the outer gap physics, were made by Cheng et al. (1986b) and Ho (1989). The latter employed a self-consistent iterative procedure with one varying parameter, the ratio of gap height and curvature radius of the field lines, and it is interesting to note that the calculated high-energy spectrum bears reasonably good overall simularity with the observed one (cf. Fig. 4 of Ho 1989 with Fig. 9 of this paper). Ulmer et al. (1995) compared the outer gap model of Ho with an early CGRO spectrum of the Crab (combining OSSE, COMPTEL and EGRET spectra) and found also good overall agreement. Chiang & Romani (1994) made refinements to the above calculations and attempted to model the Crab Total Pulse spectrum and the spectral variation with phase, which they considered to be a clear mapping of location in the magnetosphere to pulse-phase. They divided the outer gap in different sub-zones taking into account the transport of radiation and particles from sub-zone to sub-zone. Convergence to a self-consistent solution, however, resulted in spectra significantly lacking photon flux below several GeV. Romani (1996) described a revised picture of gap closure and radiation physics in the outer magnetosphere to overcome difficulties in the schema of Cheng et al. (1986b), and also addressed spectral variations with pulsar phase from the optical to the high-energy γ-ray spectrum. For the Crab pulsar, he made some qualitative statements on the expected spectral properties. He expects a significant contribution of synchrotron photons to the high-energy γ-ray flux. This could probably explain the observed underlying power-law component from soft X-rays up to high-energy γ-rays, although the observed photon index of ~ 2 is considerably softer than the expected value of ~ 1.

Building on the work of Romani and co-workers, Cheng et al. (2000) also used a three-dimensional pulsar magnetosphere to study the geometry of outer magnetospheric gap accelerators. However, the physics of both models is strikingly different. For the single outer gap model (Chiang & Romani 1994), the emission comes from the outward direction in an outer gap above one pole; the emission regions for the two peaks of the pulse profile are those close to the null-charge surface and to the light cylinder radius, respectively. In the model of Cheng et al. (2000), photon emission consists of emission outward and inward from regions in outer gaps above both poles, the gaps being limited along the azimuthal direction by $e^{\pm}$ pair production of inward-flowing photons from the outer gap. It is shown that both models can produce the same (Crab-like) pulse profiles. Cheng et al. (2000) also calculated phase-resolved spectra of the Crab pulsar. They determined the locations of the emission regions in the outer gaps in the open field line zone of the Crab magnetosphere as a function of pulse-phase. It can be seen in their Fig. 9 that high-energy emission from the P1 interval is produced high in the magnetosphere ($0.8 < r/R_{\mathrm{lc}} < 1.0$) where

curvature radiation dominates, resulting in a spectrum which extends to the GeV regime. In the interval between the pulses (TW1 and Bridge interval) high-energy radiation is predominantly produced deep in the magnetosphere where a soft synchrotron component is expected to dominate, roughly in accordance with the observations. Moving towards the P2 interval, emissions from regions high and low in the magnetosphere contribute, resulting in a overall spectrum composed of a hard curvature component and a much softer synchrotron component. In the P2 interval high-energy radiation is coming, in essence, from emitting regions extending from ∼0.2 R_{lc} to ∼1.0 R_{lc} which gives rise to a hard spectral component extending into the GeV domain and a soft component. Crossing the bridge interval moving from P1 to P2 a gradual decrease from ∼0.6 R_{lc} to ∼0.2 R_{lc} is seen for the lower bound of the emission region in the outer gap. According to Eq. (33) of Cheng et al. (2000) the dominating synchrotron emission from these regions deep in the outer gap in the pulsar's magnetosphere becomes increasingly intense moving towards P2, because the magnetic field strength becomes stronger deeper in the magnetosphere. This offers an explanation for the observed phase dependence of the bridge/broad bump spectral component, shown in Fig. 11. Beyond P2 (and before P1) this soft synchrotron component should be absent which is in agreement with the observations. Thus the model proposed by Cheng et al. (2000) seems to provide a viable and promising theoretical description of the physics responsible for the production of the Crab high-energy radiation with characteristics as shown in Figs. 9–11. A direct quantitative confrontation of this model with our observed 0.1 keV–10 GeV phase-resolved spectra is therefore strongly recommended. Cheng et al. (2000) compared in their paper the model calculations with phase-resolved Crab spectra from EGRET (>30 MeV, Fierro et al. 1998). By mistake, EGRET spectra from the phase-resolved spatial analysis were used, which also comprise the underlying nebula component. This explains the large discrepancies between the model calculations and the observed spectra for energies between 30 and 100 MeV. Cheng et al. (2000) also show a broad-band (0.1 keV–10 GeV) model spectrum for the phase-averaged Crab pulsar spectrum, which can be compared with our spectrum in Fig. 9. The overall shape of the model spectrum follows the observed spectral characteristics well, although for energies below ∼100 keV the model underestimates the observed X-ray fluxes, i.e. it seems that the component which we empirically described as a narrow spectral "bump" peaking around 20 keV in an $E^2 \times F$ representation, is not accounted for. This can be best studied in the phase-resolved analysis.

Future observations of the Crab pulsar by high-energy missions are important. In particular the spectral characteristics in the 300–1000 keV interval must be determined much more accurately. Here, data from both IBIS and SPIE aboard INTEGRAL will contribute significantly. At high γ-ray energies data from the AGILE and GLAST missions can provide sufficient statistical precision to study the peculiar spectral behaviour in the LW2 phase interval in much more detail for energies above 1 GeV. Moreover, these instruments can, for the first time, study the pulsed emission for energies above 10 GeV (upper bound of the sensitivity window is 50 GeV and 300 GeV for AGILE and GLAST, respectively). At medium γ-ray energies there are plans for a mission with an advanced, more sensitive Compton telescope (called MEGA 0.5–50 MeV; see Kanbach 2001), but no approval for such a mission exists at this time. It is just in this energy range, where interesting spectral transitions occur and where we have indications for enhanced pulsed emission in the 10–15 MeV range. Future space borne Compton telescopes having 10–100 times better sensitivity than CGRO COMPTEL are required to allow further progress.

Appendix A: Uncertainties in the absolute flux measurements at hard X-rays/soft γ-rays

In this work we compiled Crab spectra from soft X-rays up to high-energy gamma rays in order to better determine its spectral characteristics. Meanwhile, the Crab is used by many instruments as an in-flight calibration source. However, how well do we know the genuine Crab spectrum? At lower X-ray energies the measurement of the spectrum is coupled to an estimate of the N_H value, at harder X-rays up to the gamma-ray regime we have direct measurements of the Crab spectrum, but how realistic are the estimates of the accuracy of the pre-launch instrument calibrations? Is there any for which we can trust the claimed accuracies most? In this Appendix we show the present status of our knowledge of the Crab spectrum. The still large (see below) systematic differences between different instruments should be kept in mind, not only when drawing conclusions on Crab results, but for any other source in high-energy astrophysics.

In Sect. 7.1 we derived a N_H value of $3.61(2) \times 10^{21}$ cm^{-2}. This estimate is significantly larger than the N_H value of $3.23(2) \times 10^{21}$ cm^{-2} derived recently by Massaro et al. (2000) analysing a much larger BeppoSAX Crab database. The apparent discrepancy can be explained by their use of an older version of the LECS response description in combination with fitting LECS 0.1–4 keV data only, thus constraining to a lesser extent the photon index. We verified this by reproducing our values for N_H, the normalization and the photon index for this Off Pulse emission repeating our analysis for the database used by Massaro et al. (2000). From this comparison it is clear that the uncertainty in N_H is dominated by systematic uncertainties in the response characteristics, of the LECS in particular, rather than by statistical ones.
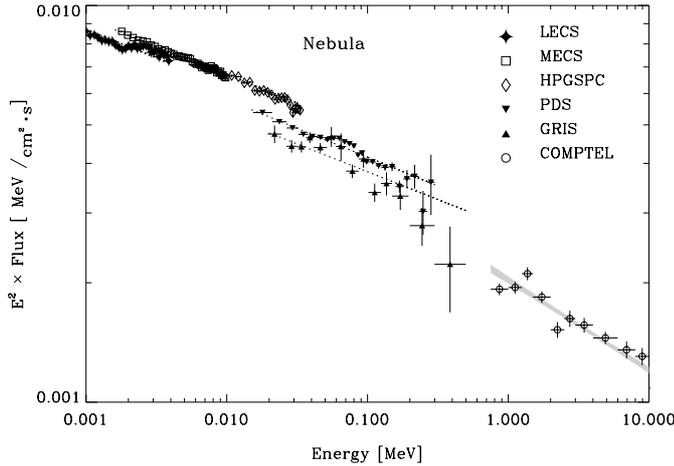
Fig. A.1. The Crab nebula spectrum in the 1 keV–10 MeV energy interval. Flux measurements from BeppoSAX LECS (1–4 keV), MECS (1.6–10 keV), HPGSPC (10–32 keV) and PDS (15–300 keV), GRIS (20–500 keV) and COMPTEL (0.75–10 MeV) are shown. The dotted lines show the best power-law fits for the combined BeppoSAX instruments and for GRIS. Note the apparent systematic deviation from the power-law fit in the LECS spectral data. The shaded band indicates the $\pm 1\sigma$ uncertainty interval around the optimum power-law fit for COMPTEL (0.75–30 MeV). Clear discrete jumps are visible between the various BeppoSAX instruments and GRIS reflecting uncertainties in absolute sensitivity.

Our value for N_{H} of $3.61(2) \times 10^{21}$ cm^{-2} is consistent with the X-ray based value of $3.45(42) \times 10^{21}$ cm^{-2} obtained by Schattenburg & Canizares (1986) using the Focal Plane Crystal Spectrometer on the Einstein observatory and with a radio based estimate of $\sim 3.65 \times 10^{21}$ cm^{-2} (Dickey & Lockman 1990). Recently, a study using XMM Newton EPIC MOS data yields a hydrogen column density of $3.45(2) \times 10^{21}$ cm^{-2} for an oxygen-iron depleted abundance of 0.63(1) solar (Willingale et al. 2001). Assuming solar abundances the N_{H} value lowers to $3.28(2) \times 10^{21}$ cm^{-2}. These estimates indicate that the genuine value of N_{H} will very probably lie in the range $(3.3 - 3.6) \times 10^{21}$ cm^{-2}.

In the fit to the data of the 4 BeppoSAX NFI instruments we derived for the sensitivity normalization scale factors, relative to the MECS (factor set to 1): LECS 0.93, HPGSPC 1.01 and PDS 0.87. This means that the LECS and PDS calibrations of their overall sensitivities deviate from that of the MECS by 7% and 13%, respectively. This is clearly visible in Fig. A.1, which presents the nebula spectrum in an $E^2 \times F$ representation between 1 keV and 10 MeV as measured with the 4 BeppoSAX NFI instruments and COMPTEL, in which no normalization correction factors have been applied. Also shown is the Crab nebula spectrum in the 0.02–1 MeV energy range as measured by the balloon borne GRIS (Ge detectors; Bartlett et al. 1994a). The combined BeppoSAX spectra as well as the GRIS spectrum are best fitted with a power-law spectral shape with a consistent slope of ~ 2.14 over the 1–700 keV interval. However, the normalization factor for

GRIS, relative to the MECS is even as low as 0.78, to be compared with the estimated GRIS systematic uncertainties of $+12\%$ and -6% by Bartlett (1994b). Allowing spectral curvature in the multi-instrument BeppoSAX nebula fit by introducing an energy dependent power-law index does not improve the fit significantly. The same is true for the GRIS spectrum. However, some gradual softening above a few 100 keV is required to connect to the softer spectrum measured by COMPTEL at energies above 1 MeV (cf. Fig. A.1; power-law photon index in the 0.75–30 MeV interval is 2.227 ± 0.013). The statistical uncertainties in the above quoted normalization correction factors are typically better than 1%. Therefore, it is obvious that the differences in absolute normalizations are systematic, and it is discouraging to note that between the two instruments for which the calibrations were expected to be most accurate (MECS and GRIS), the discrepancy appears to be largest. We cannot decide unambiguously on this controversy. Therefore, we feel that in the presentation and analysis of the above spectral data in combined broad-band spectra, this problem should not be hidden by making arbitrary choices on normalization.

References

Agrinier, B., Masnou, J. L., Parlier, B., et al. 1990, ApJ, 355, 645

Aharonian, F. A., Akhperjanian, A. G., Barrio, J. A., et al. 1999, A&A, 346, 913

Aharonian, F. A., Akhperjanian, A. G., Barrio, J. A., et al. 2000, ApJ, 539, 317

Albats, P., Frye, G. M. Jr., Zych, A. D., et al. 1972, Nature, 240, 221

Arzoumanian, Z., Nice, D., & Taylor, J. H. 1992, GRO/radio timing data base (Princeton University)

Bartlett, L. M., Barthelmy, S. D., Gehrels, N., et al. 1994, in The Second COMPTON Symp., College Park MD, 1993, ed. C. E. Fichtel, N. Gehrels, & J. P. Norris, AIP Conf. Proc., 304, 67

Bartlett, L. M., Ph.D. Thesis, The University of Maryland

Bennett, K., Bignami, G. F., Boella, G., et al. 1977, A&A, 61, 279

Borione, A., Catanese, M. A., Chantell, M. C., et al. 1997, ApJ, 481, 313

Boella, G., Chiappetti, L., Conti, G., et al. 1997, A&AS, 122, 327

Bradt, H., Rappaport, S., Mayer, W., et al. 1969, Nature, 222, 728

Browning, R., Ramsden, D., & Wright, P. J. 1971, Nature, 232, 99

Buccheri, R., Bennett, K., Bignami, G., et al. 1983, A&A, 128, 245

Carramiñana, A., Bennett, K., Buccheri, R., et al. 1994, A&A, 290, 487

Cheng, K. S., Ho, C., & Ruderman, M. 1986a, ApJ, 300, 500

Cheng, K. S., Ho, C., & Ruderman, M. 1986b, ApJ, 300, 522

Cheng, K. S., Ruderman, M., & Zhang, L. 2000, ApJ, 537, 964

Chiang, J., & Romani, R. W. 1994, ApJ, 436, 754

Clear, J., Bennett, K., Buccheri, R., et al. 1987, A&A, 174, 85

de Jager, O. C., Harding, A. K., Michelson, P. F., et al. 1996, ApJ, 457, 253

Daugherty, J. K., & Harding, A. K. 1982, ApJ, 252, 337
Daugherty, J. K., & Harding, A. K. 1994, ApJ, 429, 325
Daugherty, J. K., & Harding, A. K. 1996, ApJ, 458, 278
Dickey, J. M., & Lockman, F. J. 1990, ARA&A, 215
Eikenberry, S. S., & Fazio, G. G. 1997, ApJ, 476, 281
Everett, J. E., & Weisberg, J. M. 2001, ApJ, 553, 341
Fierro, J. 1995, Ph.D. Thesis, Stanford University
Fierro, J., Michelson, P. F., Nolan, P. L., et al. 1998, ApJ, 494, 734
Fritz, G., Henry, R. C., Meekins, J. F., et al. 1969, Science, 164, 709
Frontera, F., Costa, E., dal Fiume, D., et al. 1997, A&AS, 122, 357
Graser, U., & Schönfelder, V. 1982, ApJ, 263, 677
Gull, T. R., Lindler, D. J., Crenshaw, D. M., et al. 1998, ApJ, 495, L51
Harnden, F. R., & Seward, F. D. 1984, ApJ, 283, 279
Hasinger, G. 1984, Ph.D. Thesis, Ludwig-Maximilians-Universität München
Hasinger, G. 1985, in The Crab Nebula and Related Supernova Remnants, ed. Kafatos, & Henry (Cambridge University Press)
Hillas, A. M., Akerlof, C. W., Biller, S. D., et al. 1998, ApJ, 503, 744
Hillier, R. R., Jackson, W. R., Murray, A., et al. 1970, ApJ, 162, L177
Ho, C. 1989, ApJ, 342, 396
Kanbach, G. 2001, AIP Conference Proc. of the "Gamma 2001" Conference, Baltimore, April 2001, ed. N. Gehrels, C. Shrader, & S. Ritz, in press (see also http://www.gamma.mpe-garching.mpg.de/MEGA/mega/mega/mega.html)
Knight, F. K. 1982, ApJ, 260, 538
Kniffen, D. A., Hartman, R. C., Thompson, D. J., et al. 1974, Nature, 251, 397
Kurfess, J. D. 1971, ApJ, 168, L39
Lessard, R. W., Bond, I. H., Bradbury, S. M., et al. 2000, ApJ, 531, 942
Mahoney, W. A., Ling, J. C., & Jacobson, A. S. 1984, ApJ, 278, 784
Manzo, G., Giarrusso, S., & Santangelo, A. 1997, A&AS, 122, 341
Massaro, E., Feroci, M., Costa, E., et al. 1998, A&A, 338, 184
Massaro, E., Cusumano, G., Litterio, M., et al. 2000, A&A, 361, 695
McBreen, B., Ball, S. E. Jr., Campbell, M., et al. 1973, ApJ, 184, 1973
Mineo, T., Cusumano, G., Segreto, A., et al. 1997, A&A, 327, 21
Moffett, D. A., & Hankins, T. H. 1999, ApJ, 522, 1046
Much, R., Bennett, K., Buccheri, R., et al. 1995, A&A, 299, 435
Much, R., Bennett, K., Winkler, C., et al. 1997, Proceedings of the fourth Compton Symp. (Williamsburg, VA), ed. C. D. Dermer, M. S. Strickman, & J. D. Kurfess, AIP Conf. Proc., 410

Much, R., Carramiñana, A., & Fordham, J. L. A. 2000, ASP Conf. Ser., 202, 85, in Pulsar Astronomy – 2000 and beyond: IAU Colloq., 177
Nolan, P. L., Arzoumanian, Z., Bertsch, D. L., et al. 1993, ApJ, 409, 697
Oser, S., Bhattacharya, D., Boone, L. M., et al. 2001, ApJ, 547, 949
Parlier, B., Agrinier, B., Forichon, M., et al. 1973, Nat. Phys. Sci., 242, 117
Parmar, A. N., Martin, D. D., Favata, F., et al. 1997, A&AS, 122, 309
Pravdo, S. H., & Serlemitsos, P. J. 1981, ApJ, 246, 484
Pravdo, S. H., Angelini, L., & Harding, A. K. 1997, ApJ, 491, 808
Ramanamurthy, P. V. 1994, A&A, 284, L13
Romani, R. W. 1996, ApJ, 470, 469
Romani, R. W., & Yadigaroglu, I. A. 1995, ApJ, 438, 314
Schattenburg, M. L., & Canizares, C. R., ApJ, 301, 759
Schönfelder, V., Aarts, H., Bennett, K., et al. 1993, ApJS, 86, 657
Graham-Smith, F., Dolan, J. F., Boyd, P. T., et al. 1996, MNRAS, 282, 1354
Sollerman, J., Lundqvist, P., Lindler, D., et al. 2000, ApJ, 537, 861
Sturner, S. J., & Dermer, C. D. 1994, ApJ, 420, L79
Tanimori, T., Sakurazawa, K., Dazeley, S. A., et al. 1998, ApJ, 492, L33
Thompson, D. J., Fichtel, C. E., Hartman, R. C., et al. 1977, ApJ, 213, 252
Thompson, D. J., Bertsch, D. L., Fichtel, C. E., et al. 1993, ApJS, 86, 629
Thompson, D. J., Bertsch, D. L., Dingus, B. L., et al. 1995, ApJS, 101, 259
Tompkins, W. F., Jones, B. B., Nolan, P. L., et al. 1997, ApJ, 487, 385
Toor, A., & Seward, F. D. 1977, ApJ, 216, 560
Ulmer, M. P., Lomatch, S., Matz, S. M., et al. 1994, ApJ, 432, 228
Ulmer, M. P., Matz, S. M., Grabelsky, D. A., et al. 1995, ApJ, 448, 356
Vacanti, G., Cawley, M. F., Colombo, E., et al. 1991, ApJ, 377, 467
van der Meulen, R. D., Bloemen, H., Bennett, K., et al. 1998, A&A, 330, 321
Walraven, G. D., Hall, R. D., Meegan, C. A., et al. 1975, ApJ, 202, 502
Wills, R. D., Bennett, K., Bignami, G. F., et al. 1982, Nature, 296, 723
Willingale, R., Aschenbach, B., Griffiths, R. G., et al. 2001, A&A, 365, L212
Yadigaroglu, I.-A. 1997, Ph.D. Thesis, Stanford University
Zhang, B., & Harding, A. K. 2000, ApJ, 532, 1150